JOURNAL OF MATERIALS SCIENCE **34** (1999) 1211 – 1218

Spray atomization of two Al–Fe binary alloys: solidification and microstructure characterization

J. JUAREZ-ISLAS
Instituto de Investigaciones en Materiales, UNAM, Apdo Postal 70-360, Mexico D. F. 04510, Mexico

Y. ZHOU, E. J. LAVERNIA
Department of Chemical and Biochemical Engineering and Materials Science, University of California, Irvine, CA 92697-2575, USA
E-mail: lavernia@uci.edu

The effect of solidification history on the resultant microstructures in atomized Al–3Fe and Al–7Fe powders is studied, with particular emphasis on the relationships between droplet size, undercooling and phase stability. The atomized Al–Fe powders exhibit four microstructural features, i.e. Al_3Fe phase, $Al + Al_6Fe$ eutectic, α-Al dendrite and a predendritic structure. The presence of these is noted to depend on a kinetic phase competitive growth mechanism, which was determined by the initial undercooling experienced by the powders. The results of scanning electron microscope analysis demonstrate that the content of Fe in the α-Al phase increases with decreasing powder particle size, i.e. for Al–3 wt % Fe powders, the content of Fe in the α-Al phase is 2.21 and 2.56 wt % corresponding to powder particle sizes of 90 and 33 μm, respectively; for Al–7 wt % Fe powders, the content of Fe in the α-Al phase is 5.51 and 5.98 wt % corresponding to powder sizes of 90 and 33 μm, respectively. In the present study, homogeneous nucleation undercooling, corresponding to the α-Al phases, is also estimated using an existing correlation.

1. Introduction

The extent of undercooling during solidification of metals plays a critical role in microstructural evolution by dictating phase selection. Among the available techniques that may be effectively used to enhance the degree of undercooling during solidification, atomization remains a popular choice as a result of its versatility and potential for tonnage production [1]. For example, a single atomization experiment may be used to generate a wide range of powder sizes with concomitant variation in solidification conditions [2, 3]. Control of the amount of undercooling prior to solidification may be effectively utilized to promote the formation of non-equilibrium phases and highly refined microstructures, with concomitant benefits to mechanical behaviour. Increasing the extent of undercooling may expand the range of available phases by allowing competitive nucleation and growth [4–6]. Accordingly, an understanding of the factors that control the extent of undercooling may be helpful to tailor the microstructure.

The Al–Fe system is of interest for several reasons. First, when solidified in the presence of a high undercooling, this system forms several dispersoids of Al_xFe type [7–9]. Second, this system constitutes the basis of a family of commercially important elevated temperature Al alloys due to the very low equilibrium solid solubility and very low diffusion rate of Fe in Al [10, 11]. The microstructure and phase stability of Al–Fe alloys are strongly influenced by the extent of undercooling during solidification [12–14] as well as by the concentration of Fe [15]. For example, under identical solidification conditions lowering the Fe content can result in a more homogeneous microstructure and finer primary Al_xFe particles [15]. In addition, the content of Fe has an effect on the relative stability of the metastable Al_6Fe phase and the stable Al_3Fe phase [16]. It has been well documented [12–14, 16] that two distinct types of microstructure coexist in Al–Fe powders, i.e. a microeutectic or microcellular structure (Zone A) and a dendritic structure (Zone B). Moreover, the presence of a high undercooling can suppress or, at least reduce, the formation of some primary phases [17]. The objective of the present investigation was to enhance the understanding of the effect of the solidification condition on the resultant microstructure and phase stability of Al–Fe alloys. The resultant microstructures were analysed, on the basis of related nucleation and growth theories. Particular emphasis was placed on elucidating the relationships between droplet size, undercooling and microstructure.

2. Experimental procedure

Two alloys with nominal compositions of Al–3 wt % Fe (designated as Al–3Fe) and Al–7 wt % Fe (designated

TABLE I Experimental variables and specific diameters of atomized powders

Variables	Values	
	Al–3Fe	Al–7Fe
Fe, wt %	3.23	7.01
Superheat temperature, K	1053	1143
Atomization gas	N_2	N_2
Atomization gas pressure, MPa	1.55	1.97
Gas flow rate, kg s^{-1}	0.024	0.029
Metal flow rate, kg s^{-1}	0.028	0.029
d_{16}, μm	46	34
d_{50}, μm	109	85
d_{84}, μm	263	232

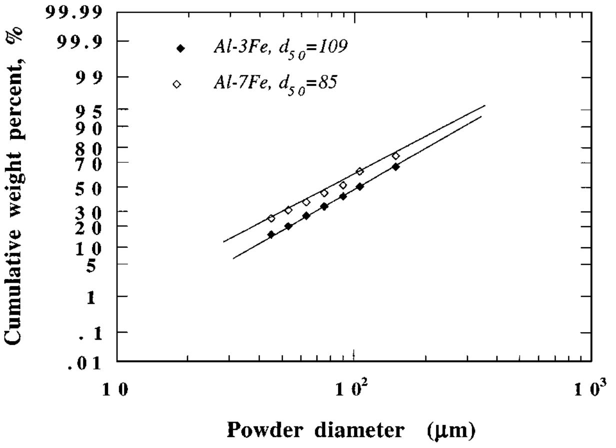

Figure 1 Size distribution of atomized Al–Fe powders.

as Al–7Fe) were selected. The alloys were prepared using pure Al (99.99%) and Fe (99.98%). In the atomization experiments, the alloys were first superheated to temperatures of 200 K above the equilibrium liquidus, and maintained for 1 h to ensure complete dissolution of all the primary phases. The alloys were then cooled down to superheat temperatures of 90 K above the liquidus, and atomized into a distribution of micrometre-sized droplets using nitrogen gas. To reduce oxidation, the experiments were conducted inside an environmental chamber, which was evacuated down to a pressure of 100 Pa and backfilled with nitrogen to a pressure of 1.05×10^5 Pa prior to melting and atomization. The primary atomization variables used in the present study are listed in Table I. It should be noted that in order to compensate for the differences in melting temperatures between Al–3Fe and Al–7Fe and hence the differences in superheat temperature, the latter material was atomized using a slightly higher atomization pressure (1.97 MPa) relative to the former (1.55 MPa).

The atomized Al–Fe powders were collected, and the real content of Fe was determined using direct current plasma emission spectroscopy method (Luvak Inc., Boylston, MA). Powder particle size distributions were established by mechanical sieving according to ASTM standard B214 and MPIF standard 5. The powders were then mounted for microstructural analyses using standard metallographic techniques. Keller's reagent (2.5% NHO_3 : 1.5% HCl : 0.5% HF : H_2O) was used to reveal microstructural features.

The phases that were present in the powders were identified by X-ray diffractometry (XRD). The X-ray measurements were conducted in a Siemens D5000 diffractometer using CuK_{α_1} radiation with a wavelength $\lambda = 0.15406$ nm. XRD spectra were determined in the $2\theta = 10$–130° range with a resolution of 0.02° and a time step of 2 s.

Characterization of the morphology of the various phases present and microanalysis of the Fe content in specific phases were conducted using a scanning electron microscope (SEM). The SEM studies were also carried out to measure the secondary dendrite arm spacing (SDAS) in the atomized powders, and accordingly, to determine the cooling rate the powders experienced using an empirical equation.

3. Results and discussion

3.1. Particle size distribution of atomized Al–Fe powders

In the atomization of metals, droplet size and distribution may significantly impact the thermal history of droplets as well as solidification characteristics of droplets during flight. Therefore, a knowledge of droplet size and distribution is required to facilitate understanding of solidification and the resultant microstructure. The size distributions for Al–3Fe and Al–7Fe powders were established by summarizing the results of the sieving experiments in a probability graph of cumulative weight percentage versus powder diameter. The results summarized in Fig. 1 show that the size distribution of the atomized powders may be approximated by a logarithmic-normal function. Based on a logarithmic-normal relationship, the mass median powder diameter (d_{50}) was determined to be 109 μm for the Al–3Fe alloy and 85 μm for the Al–7Fe alloy, respectively. The specific powder sizes, d_{16} and d_{84}, which corresponded to the opening of a screen mesh that let through 16 and 84 wt % of the powders, respectively, were also determined and summarized in Table I. There was a difference in mass median diameter d_{50} between the Al–3Fe and the Al–7Fe powders. The value of d_{50} for Al–7Fe powders was smaller than that of Al–3Fe powders. It is well recognized [18–21] that the powder size distribution produced by the atomization process is closely related to the operating variables, such as ratio of gas to liquid flow rate and physical properties and chemical properties of the liquid and atomizing gas. The Lubanska equation [20] is a typical empirical correlation commonly used for atomization of metals, which shows that the mass median diameter of powders (D_m or d_{50}) is inversely proportional to the gas–liquid flow ratio, J_g/J_l

$$\frac{D_m}{D_o} = K_a\left[\frac{\nu_l}{\nu_g W_e}\left(1 + \frac{J_l}{J_g}\right)\right]^{0.5} \tag{1a}$$

and

$$W_e = \frac{V_g^2 \rho_l D_o}{\gamma_l} \tag{1b}$$

where D_o is the liquid stream diameter; K_a is an experimentally determined constant; ν_l and ν_g are the kinematic viscosities of the liquid and atomizing gas, respectively; γ_l is the interfacial energy of the liquid; ρ_l is the density of the liquid; W_e is Weber's number; and v_g is gas velocity. In the present study, a higher atomizing gas pressure was used for Al–7Fe alloy to compensate for the difference in atomizing temperature between Al–3Fe and Al–7Fe alloys. Therefore, the atomizing gas flow rate in atomization of Al–7Fe powders was higher than that of Al–3Fe powders, as shown in Table I. Accordingly, the ratio of gas to liquid flow rate (1.0) for Al–7Fe powder was larger than that (0.857) for Al–3Fe powder. Consistent with the other studies [18–21], the present results demonstrate that the mass median diameter decreases with increasing ratio of gas to liquid flow rates. Another parameter that can represent the spread of powder size distribution is the standard deviation, which can be expressed as $\sigma = d_{84}/d_{50}$, assuming that powder size obeys a log normal distribution. Comparison of the standard deviation for Al–3Fe ($\sigma = 2.41$) and Al–7Fe ($\sigma = 2.73$) indicated that a higher gas pressure (Al–7Fe) resulted in a broader size distribution.

3.2. Cooling rate and solidification behaviour of atomized powders

In the case of powders exhibiting a primary dendritic morphology, the secondary dendrite arm spacing (SDAS) was measured for each powder size range. The average SDAS corresponding to each powder size range was graphed as a function of powder size. The results, shown in Fig. 2, indicate that the SDAS decreases with decreasing powder size. The measured SDAS were then used to calculate average cooling rates experienced by the powders during solidification according to the empirical relationship proposed by Ahlborn and Merz [22] for the Al-Fe alloy system

$$\text{SDAS} = 77\,\dot{T}^{-0.42}(\mu\text{m}) \tag{2}$$

where $\dot{T}$ is the cooling rate (K s^{-1}). The results of these calculations, which are also summarized in Fig. 2, show that the cooling rates increase significantly with decreasing powder size. The cooling rates of the Al–7Fe powders were generally higher than those of the Al–3Fe powders. Accordingly, the Al–7Fe powders showed a finer secondary dendrite arm spacing. This difference on cooling rate may be rationalized on the basis of the slightly higher heat transfer coefficient that was associated with the higher atomization gas pressure (1.97 MPa) used for the Al–7Fe powders as compared with that (1.55 MPa) used for the Al–3Fe powders [23].

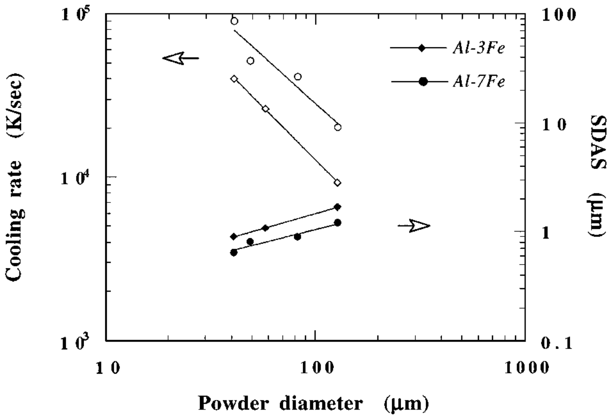

Figure 2 Measured secondary dendrite arm spacings (SDAS) and calculated cooling rates as a function of powder sizes for atomized Al–Fe powder particles.

It is known [24] that one of the characteristics of rapid solidification is the attainment of relatively high levels of undercooling prior to the onset of nucleation. Atomization may be used to attain high levels of undercooling while simultaneously promoting rapid rates of thermal energy transfer, and thereby high cooling rates. These conditions are typically used to rationalize the presence of a refined solidification morphology, e.g. small SDAS, and the formation of non-equilibrium microstructures, e.g. extended solid solutions, that are commonly reported for atomized powders. The following discusses the homogeneous undercooling and its estimation for the current study using previous results.

The homogeneous undercooling corresponds to the maximum level of undercooling that may be achieved by metallic droplets prior to solidification, under given environmental conditions such as droplet size and cooling rate. The extent of undercooling that is necessary for homogeneous nucleation in a spherical droplet may be calculated on the basis of droplet size and cooling rate by the following equation [25]

$$\Delta T_{\text{hom}}^2 = \frac{16\pi\sigma_{\text{m}}^3\Omega^2T_{\text{l}}^2}{3kT_{\text{n}}H_{\text{f}}\ln\left[4\pi \times 10^{-2}D\left(\frac{r^*}{a}\right)^2\left(\frac{a}{\Omega}\right)\left(\frac{V\Delta T_{\text{hom}}}{10^2\dot{T}}\right)\right]} \tag{3}$$

where V is the volume of the undercooled droplet (in cubic metres), r^* is the critical radius of the nucleus (metres); a is the atomic diameter (metres); D is the liquid diffusivity (square metres per second); σ_m is the solid–liquid interfacial energy (Joules per square metre); Ω is the atomic volume (cubic metres per atom); k is the Boltzmann constant (Joules per atom per kelvin); H_f is the latent heat of fusion (Joules per mole); T_l is the equilibrium liquidus temperature (Kelvins); and T_n is the nucleation temperature (Kelvins). It should be noted that the magnitude of the prefactor in Equation 3, $4\pi \times 10^{-2}D(r^*/a)^2\,(a/\Omega)$, normally falls in the range 10^{41}–10^{46} ($\text{m}^{-3}\ \text{s}^{-1}$) [25]. An experimentally determined value, 10^{46} ($\text{m}^{-3}\ \text{s}^{-1}$), was chosen in the present investigation. Therefore, Equation 3 reduces to

$$\Delta T_{\text{hom}}^2 = \frac{16\pi\sigma_{\text{m}}^3\Omega^2T_{\text{l}}^2}{3\,kT_{\text{n}}H_{\text{f}}\ln\left[10^{44}\left(\frac{V\Delta T_{\text{hom}}}{\dot{T}}\right)\right]} \tag{4}$$

Taking into account the cooling rates determined on the basis of the previous section, and using the physical constants shown in Table II, the magnitude of the homogeneous undercooling associated with the formation of the α-Al phase in the Al–3Fe and the Al–7Fe powders was calculated, and the results are summarized in Table III. These calculated results evidently indicate

TABLE II Thermodynamic parameters used in calculating the homogeneous undercooling of the Al–Fe droplets [12, 34]

Parameter	Al–3Fe	Al–7Fe
Interfacial energy, σ_m, J m^{-2}	0.121	0.121
Atomic volume, Ω, m^3 atom^{-1}	1.65×10^{-29}	1.65×10^{-29}
Equilibrium liquidus, T_l, K	938	1063
Boltzmann constant, k, J K^{-1}	1.38×10^{-23}	1.38×10^{-23}
Latent heat of fusion, H_f, J mol^{-1}	1.04×10^4	1.02×10^4
Atom diameter, a, m	3.45×10^{-10}	3.45×10^{-10}
Liquid diffusivity, D, m^2 s^{-1}	2×10^{-9}	2×10^{-9}
Specific heat of liquid, C_p, J mol^{-1} K	31.5	31.1

TABLE III Calculated cooling rates for Al–Fe powders and undercoolings of α-Al phase in Al-Fe powders

	Al–3Fe		Al–7Fe	
d(μm)	$\dot{T}$ (K s^{-1})	ΔT_{hom} (K)	$\dot{T}$ (K s^{-1})	ΔT_{hom} (K)
128	9.2×10^3	180.0	2.0×10^4	196.0
98	1.3×10^4	183.0	2.9×10^4	198.0
58	2.6×10^4	186.0	5.2×10^4	201.0
41	4.0×10^4	188.0	9.0×10^4	204.0

that the homogeneous undercooling of the droplets is dependent upon the thermal properties of the alloy, the droplet size and the cooling rate experienced by the undercooled droplets. For the Al–3Fe and Al–7Fe powders with the same size, such as 128 μm, the calculated homogeneous nucleation undercooling was 180 and 196 K, respectively. This difference resulted from the fact that: (i) Al–7Fe powders experienced a higher cooling rate compared with Al–3Fe powders under the same size category due to a difference in atomizing gas pressure, and (ii) Al–Fe alloy with higher solute content needs higher undercooling to achieve homogeneous nucleation. Inspection of the variation of undercooling with powder size demonstrates that smaller size powder experiences a higher undercooling. The effects of undercooling on the resultant microstructure will be discussed below.

3.3. Microstructure and competition of different phases in atomized powders

The results obtained from metallographic studies revealed that there were four types of microstructures present in the Al–3Fe and the Al–7Fe powders. First, as shown in Fig. 3, a fraction of the powders exhibited coarse primary phases in the matrix of α-Al. The primary phases were generally needle-like (Fig. 3a) or in some cases, blocky (Fig. 3b). This observation is consistent with the studies on rapidly solidified Al–Fe alloys [12–15] in which this primary phase was identified as the equilibrium Al_3Fe phase. The second type of microstructure exhibited an eutectic morphology, Al–Al_6Fe eutectic, as shown in Fig. 4. The Al_6Fe phases were rod-like in the Al–Al_6Fe eutectic. Fig. 5 presents the third type of microstructure, which consisted of a dendritic morphology of the α-Al phase. Finally, some of the powders exhibited a predendritic microstructure with two different rings, as shown in Fig. 6. This type of predendritic structure was found in different sizes of powders. In addition, several grains were observed in a

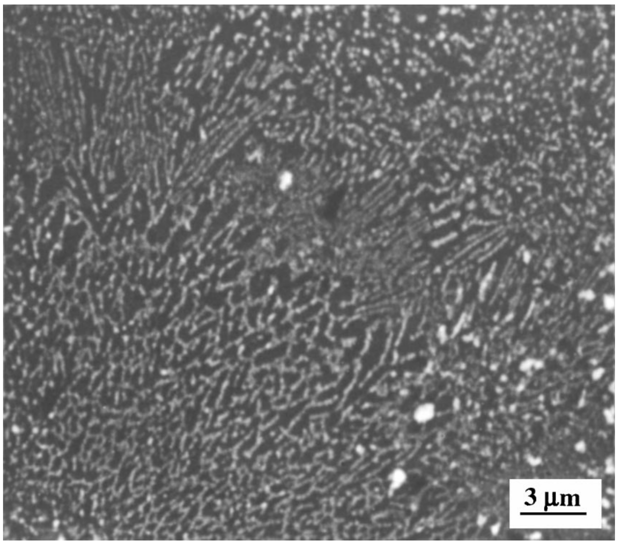

Figure 4 Microstructure of Al–7Fe powder (60 μm) showing morphology of α–Al + Al_6Fe eutectic phase (SEM).

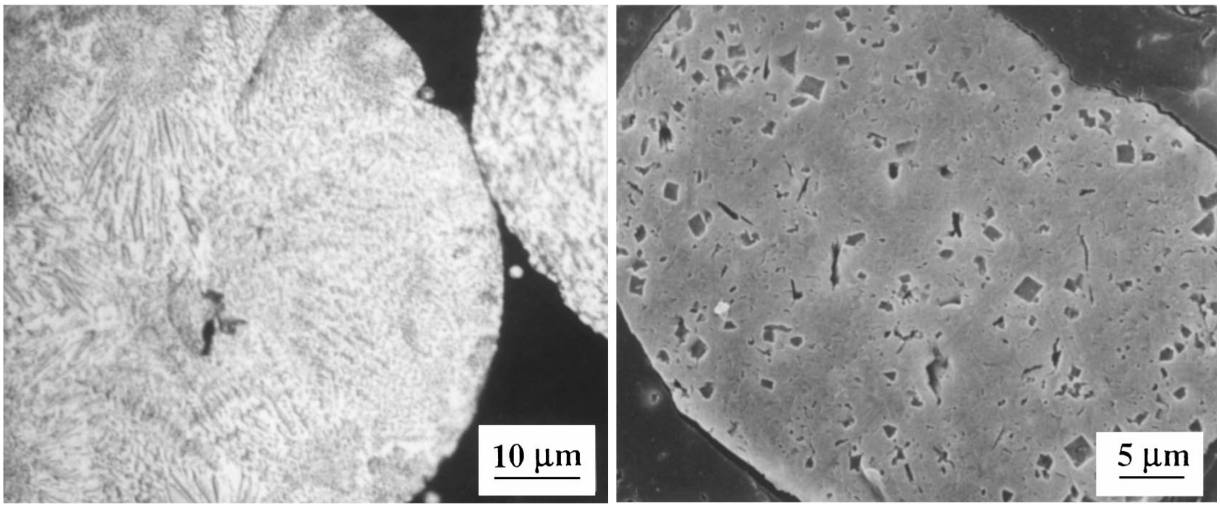

Figure 3 Microstructure of Al–7Fe powders showing different morphologies of primary phase Al_3Fe: (a) Al–7Fe (+77 μm), optical; (b) Al–Fe (+45 μm), SEM.

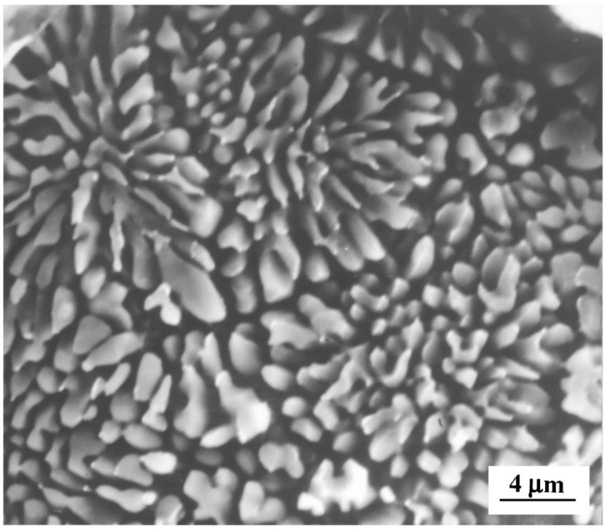

Figure 5 Microstructure of an Al–3Fe powder (90 μm) showing a dendritic morphology (SEM).

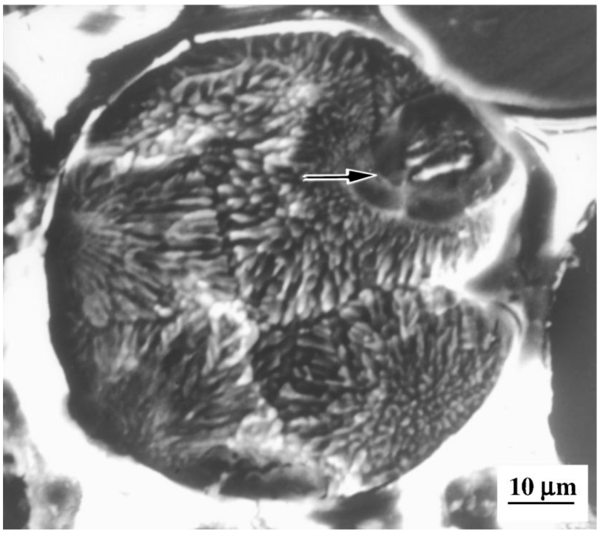

Figure 6 Microstructure of Al–3Fe powder (90 μm) showing a predendritic structure (see arrow– (SEM). Several grains are visible.

single powder as shown in Fig. 6, which also demonstrated that once the dendrite started to grow, with a cell morphology, dendrite arms developed and this sequence stopped when the fronts from different nucleation centres converged. Fig. 7 presents a grain boundary between α-Al phases at a high resolution. Fig. 8 illustrates the various morphologies of the α-Al phase as present in a single powder, which shows that large differences in local solidification conditions may occur in a single powder.

The phases that were present in the atomized Al–Fe powders were further identified by XRD analysis. Accordingly, the XRD spectra corresponding to each powder size range were compared with the standard diffraction files from each specific phase. Fig. 9 shows a typical XRD spectrum from atomized Al–7Fe powders in the size range 45–53 μm. The strong diffraction peaks were from the matrix α-Al phase, whereas the relatively weak diffraction peaks were from the intermetallic phases, e.g. Al_3Fe or Al_6Fe.

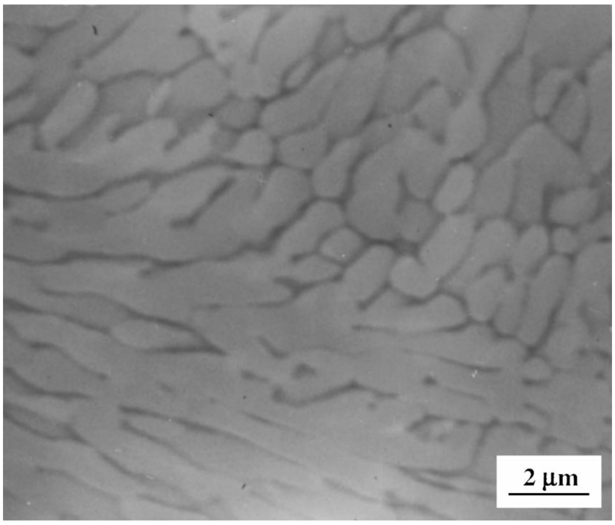

Figure 7 Microstructure indicating grain boundary in an Al–3Fe powder (33 μm, SEM).

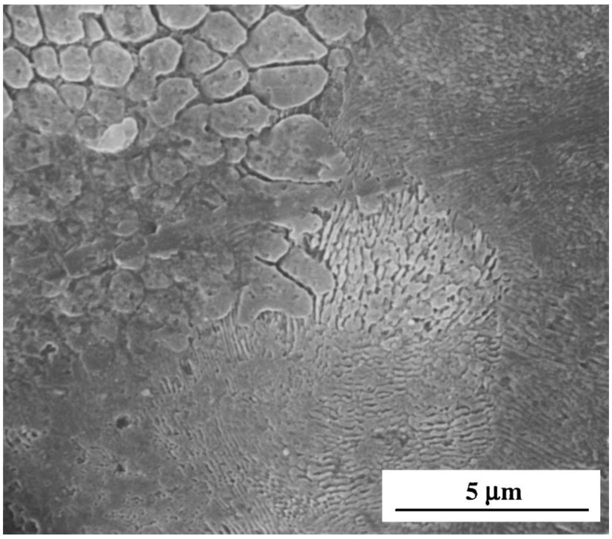

Figure 8 Microstructure of Al–7Fe powder (+45 μm) showing different morphologies of α-Al phase (SEM).

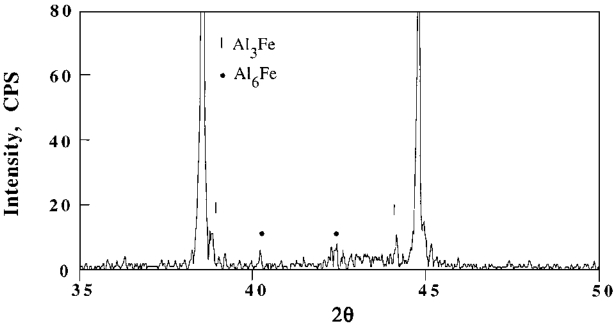

Figure 9 X-ray spectra of atomized Al–7Fe powders in the size range 45–53 μm; the strong diffraction peaks are from the matrix α–Al phase. The weak diffraction peaks from Al_3Fe and Al_6Fe are indicated in the figure.

To a certain extent, processing variables can be manipulated to control the degree of undercooling and thereby promote a transition in solidification microstructural features. The formation of various phases during atomization may be further understood on the basis of a competitive nucleation mechanism.

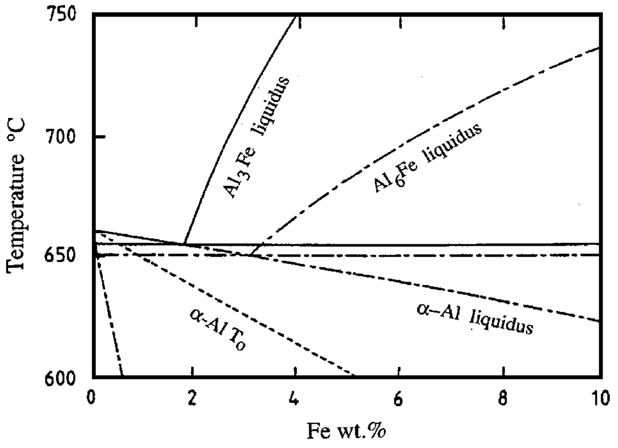

Figure 10 Al–rich side of the binary Al–Fe non-equilibrium phase diagram, calculated by Murray [28].

Perepezko [26], Bosewell and Chadwick [27], for example, elucidated how an increased cooling rate might be expected to enhance the attainment of high undercooling before nucleation of different phases using time–temperature–transformation (T–T–T) curves. It is likely that competitive continuous cooling transformation curves will involve competition among at least a few different morphologies [27]. Hence, the probability of forming a particular phase may be predicted by considering the level of undercooling achieved under high cooling rate or low cooling rate conditions. For the present Al–Fe powders, the formation of different phases may further be rationalized using a metastable phase diagram. Fig. 10 shows the Al-rich side of the binary Al–Fe phase diagram, which includes the metastable phase boundaries and α-Al lines as calculated by Murray [28]. The phase diagram indicates that the formation of a range of metastable phases and microstructural morphologies depends on the degree of initial undercooling experienced by the droplets [4–6].

It has been argued in the previous discussion that the formation of various phases is influenced by the degree of undercooling experienced by the powders. The relative amount of these phases, however, may also be affected by their growth kinetics. For example, it has been shown that at high solid–liquid interface growth velocities, the Al_6Fe phase is favoured in suppression of the Al_3Fe phase and the minimum growth velocity necessary for suppression of the Al_3Fe phase increases with Fe content [29, 30]. More recently, Gilgien *et al.* [31] summarized the relationship among the composition, interface growth rate and microstructure formation for Al–Fe alloys using a microstructure selection map. It was concluded [31] that the interface growth velocity needed for the favourable formation of Al_3Fe, Al_6Fe and α-Al phases increases sequentially, and formation of a particular phase is controlled by the interface growth rate corresponding to the undercooling. Fig. 5, in the present study, shows the α-Al + Al_6Fe phase present along the α-Al phase boundary, indicating that the α-Al phase first formed, and as the interface temperature raised due to recalescence, the α-Al + Al_6Fe phase became competitive. From Fig. 4, however, it can be seen that the α-Al + Al_6Fe phase was developed completely. The interface growth velocity of a particular phase can be related to the undercooling experienced by a powder. For dynamic solidification conditions in the Al–Fe system, Chu and Granger [32] derived a kinetic relationship between interface growth velocity, V, and undercooling, ΔT. For Al–3Fe, the relationship was approximately expressed as

$$V = 8.85 \times 10^{-6} \Delta T^{\alpha} \tag{5a}$$

and

$$\alpha = 3.66 - 0.36 \log \Delta T \tag{5b}$$

where V is in metres per second, and ΔT in kelvine. For Al–7Fe, the relationship was expressed as [32]

$$V = 5.78 \times 10^{-7} \Delta T^{\alpha} \tag{6a}$$

and

$$\alpha = 3.89 - 0.34 \log \Delta T \tag{6b}$$

Comparison of Equations 5 and 6 indicates that the extent of undercooling has a relatively strong influence on the interface velocity of α-Al in the Al–3Fe system. Assuming that the achievable initial undercooling ΔT after the onset of nucleation equals that for homogeneous nucleation, the initial interface growth velocity can be estimated using Equations 5 and 6. As shown in Fig. 11, these calculated results of the initial interface growth velocity, based on experimental data in Table III, indicate that the interface velocity increases with decreasing powder particle size because the cooling rate increases with reducing particle size. It also indicates that the composition of Fe has a significant effect on the interface velocity, supporting that compared with dilute alloys (e.g. Al–3Fe), concentrated alloys (e.g. Al–7Fe) need higher undercooling or a higher cooling rate to achieve an equivalent interface growth velocity. Note that the diffusion velocity of Fe in liquid

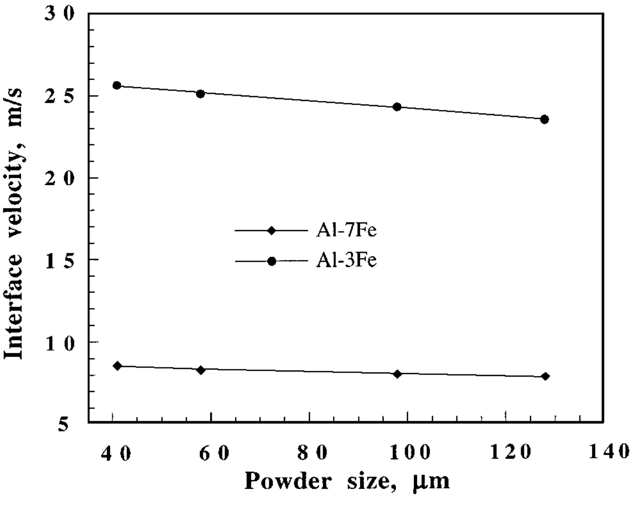

Figure 11 Interface growth velocity with different powder size for Al–3Fe and Al–7Fe powder particles.

TABLE IV Measured Fe content (wt %) in α-Al phase using SEM

	Al–3Fe			Al–7Fe		
	90 μm	55 μm	33 μm	90 μm	55 μm	33 μm
	2.19	2.53	2.69	5.47	5.72	5.96
	2.23	2.39	2.56	5.52	5.81	5.99
	2.35	2.16	2.70	5.48	5.80	5.96
	2.08	2.37	2.46	5.54	5.64	5.97
	2.14	2.43	2.56	5.48	5.76	5.99
	2.34	—	2.36	5.54	5.82	5.99
	2.15	—	—	—	—	—
Averaged	**2.21**	**2.38**	**2.56**	**5.51**	**5.76**	**5.98**

Al was estimated to be in the range of 5 ms^{-1} [12]. Partitionless solidification should, therefore, occur as the interface growth velocity is larger than the diffusion velocity, and accordingly, a microsegregation-free structure should be formed. Moreover, examination of the powder microstructure showed no direct evidence that such a microsegregation-free structure formed, indicating an absence of such a high interface growth velocity (or undercooling) achieved. This is most likely that heterogeneous nucleation was dominant due to the presence of potential catalytic sites for nucleation.

3.4. Solubility and microanalysis of Fe

Chemical analysis using plasma emission spectroscopy was carried out to determine the real composition of Fe in Al–3Fe (Al–3.23 wt % Fe) and Al–7Fe (Al–7.01 wt % Fe) atomized powders (see Table I). Table IV summarizes the measured Fe contents in the α-Al phase as determined for Al–3Fe and Al–7Fe powders of different powder sizes (33, 55 and 90 μm) using SEM microanalysis. Fig. 12, graphed on the basis of Table IV, demonstrates that for Al–3Fe and Al–7Fe powders, the content of Fe in the α-Al phase increases with decreasing powder size. For example, for Al–3Fe powders, the content of Fe in the α-Al phase is 2.21 and 2.56 wt % corresponding to powder sizes of 90 and 33 μm, respectively; for Al–7Fe powders, the content of Fe in α-Al phase is 5.51 and 5.98 wt % corresponding to powder sizes of 90 and 33 μm, respectively. It has been documented [33] that the maximum solid solubility of Fe in Al at equilibrium is 0.025 at %. In the present study, the SEM microanalysis results (Table IV) demonstrate that the solubility of Fe in the α-Al phase can be extended significantly under the investigated solidification conditions. For example, the content of Fe in the α-Al phase was 2.21 and 5.51 wt % corresponding to 90 μm powders of Al–3Fe and Al–7Fe, respectively. Note that care must be taken for microanalysis using SEM as the cell size decreases. The X-ray spot for microanalysis may cross at the grain boundaries where the α-Al + Al$_6$Fe eutectic could exist.

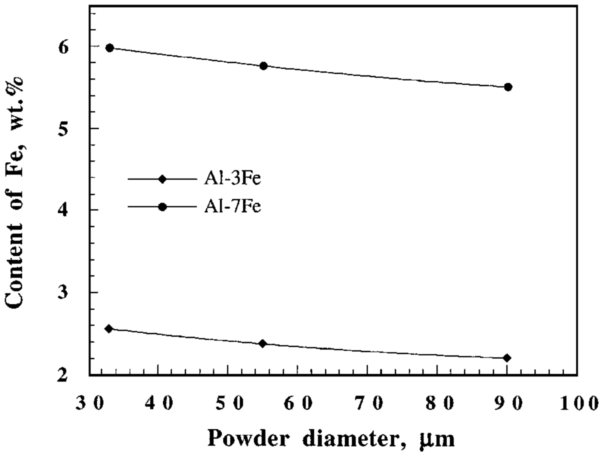

Figure 12 Variation of Fe content in α–Al phase with powder size for Al–3Fe and Al–7Fe powder particles.

The Fe content in the predendritic structure was also analysed using SEM microanalysis. The predendritic structure was formed by two zones (as shown in Fig. 6). There was a difference in Fe content between the inner and the outer zone. The averaged Fe content of the inner zone was 3.31 wt %, whereas it was 2.76 wt % for the outer zone in the predendritic structure.

4. Conclusions

In the present study, four types of microstructures in the atomized Al–Fe powders were found, Al$_3$Fe phase, Al + Al$_6$Fe eutectic, α-Al dendrite and a predendritic structure. SEM microanalysis demonstrated that the content of Fe in the α-Al phase increases with decreasing powder size such that for Al–3Fe powders, the content of Fe in the α-Al phase is 2.21 and 2.56 wt % corresponding to powder sizes of 90 and 33 μm, respectively; for Al–7Fe powders, the content of Fe in the α-Al phase is 5.51 and 5.98 wt % corresponding to powder sizes of 90 and 33 μm, respectively. The results also show that the undercooling increases with increasing cooling rate and decreasing size of the atomized powders.

Acknowledgements

Supports from NASA (Grant No. NAGI-1619) and NSF (Grant No. ARO-AASERT (Grant No. DAAG 55-98-1-0141) CTS-9614653) are gratefully acknowledged. The authors would like to thank Dr Y. Wu and Dr X. Liang for helpful discussions and for the experimental work.

References

1. A. LAWLEY, in "Processing of Structural Metals by Rapid Solidification," edited by F. H. Froes and S. J. Savage (American Society for Metals International, Metals Park, OH, Baton Rouge, LA, 1987) p. 31.
2. H. JONES, in "Rapid Solidification Processing: Principles and Technology," edited by R. Mehrabian, B. H. Kear and M. Cohen (Claitor's Publishing Division, 1978) p. 28.
3. E. J. LAVERNIA, J. D. AYERS and T. S. SRIVATSAN, *Int. Mater. Rev.* **37** (1992) 1.
4. D. TURNBULL, in "Undercooled Alloy Phases," edited by E. W. Collings and C. C. Koch (American Institute of Mining, Metallurgical and Petroleum Engineers–TMS, Warrendale, PA, 1987) p. 3.
5. J. H. PEREPEZKO, *Mater. Sci. Eng.* **A226–228** (1997) 374.

6. P. G. HÖCKEL, H. SIEBER and J. H. PEREPEZKO, in "Solidification 1998," edited by S. P. Marsh, J. A. Dantzig, R. Trivedi, W. Hofmeister, M. G. Chu, E. J. Lavernia and J.-H. Chun (The Minerals, Metals & Materials Society, Warrendale, PA, 1998) p. 289.
7. D. J. SKINNER, K. OKAZAKI and C. M. ADAM, in "Rapidly Solidified Powder Aluminum Alloys," edited by M. E. Fine and E. A. Starke, Jr (ASTM-STP 890, Philadelphia, PA, 1986) p. 211.
8. M. J. COUPER and R. F. SINGER, in "High Strength Powder Metallurgy Aluminum Alloys II," edited by G. J. Hildeman and M. J. Koczak (American Institute of Mining, Metallurgical and Petroleum Engineers–TMS, Warrendale, PA, 1986) p. 199.
9. W. G. J. BUNK, *Mater. Sci. Eng.* **A134** (1991) 1087.
10. C. SURYANARAYANA, F. H. FROES and W. E. QUIST, in "Advances in Powder Metallurgy, 1991," Vol. 6 (American Powder Metallurgy Federation, Princeton, NJ, 1991) p. 15.
11. P. S. GILMAN, R. G. RATEICK and A. TESTA, in *ibid.* p. 47.
12. W. J. BOETTINGER, L. BENDERSKY and J. G. EARLY, *Metall. Trans. A*, **17A** (1986) 781.
13. R. F. COCHRANE, P. V. EVANS and A. L. GREER, *Mater. Sci. Eng.* **A133** (1991) 803.
14. R. F. COCHRANE, S. B. NEWCOMB, P. V. EVANS and A. L. GREER, *Key Eng. Mater.* **38 & 39** (1989) 21.
15. J. D. COTTON and M. J. KAUFMAN, *Metall. Trans. A* **22A** (1991) 927.
16. C. M. ADAM, in "Rapidly Solidified Amorphous and Crystalline Alloys," edited by B. H. Kear, B. C. Giessen and M. Cohen (Elsevier, New York, 1982) p. 411.
17. J. H. PEREPEZKO, J. A. GRAVES and B. A. MUELLER, in "Processing of Structural Metals by Rapid Solidification," edited by F. H. Froes and S. J. Savage (American Society for Matals International, Metals Park, OH, 1987) p. 13.
18. E. J. LAVERNIA, T. S. SRIVATSAN and R. H. RANGEL, *Atomization and Sprays* **2** (1992) 253.
19. S. NUKIYAMA and Y. TANASAWA, *Trans. Jpn. Soc. Mech. Eng.* **5** (1939) 68.
20. H. LUBANSKA, *J. Metals* **22** (1970) 45.
21. A. H. LEFEBVRE, *J. Eng. Gas Turbines Power* **114** (1992) 89.
22. V. H. AHLBORN and D. MERZ, *Aluminium* **47** (1971) 671.
23. R. MEHRABIAN, *Int. Met. Rev.* **27** (1982) 185.
24. H. JONES, in "Rapid Solidification of Metals and Alloys" edited by H. Jones (Institution of Metallurgists, London, 1982).
25. J. P. HIRTH, *Metall. Trans. A* **9A** (1978) 401.
26. J. H. PEREPEZKO, in "Science and Technology of the Undercooled Melt," edited by P. R. Sahm, H. Jones and C. M. Adam (Martinus Nijhoff Publishers, Dordrecht, 1986) p. 29.
27. P. G. BOSEWELL and G. A. CHADWICK, *J. Mater. Sci.* **12** (1977) 1879.
28. J. L. MURRAY, in "Alloy Phase Diagrams," edited by L. H. Bennett, T. B. Massalski and B. C. Giessen (Elsevier, New York, 1983) p. 249.
29. C. M. ADAM and L. M. HOGAN, *J. Aust. Inst. Metals* **17** (1972) 81.
30. P. G. KEONG, J. A. SAMES, C. M. ADAM and R. M. SHARP, in "Solidification and Casting of Metals" (The Metals Society, London, 1979) p. 110.
31. P. GILGIEN, A. ZRYD and W. KURZ, *Acta Metall. Mater.* **43** (1995) 3477.
32. M. G. CHU and D. A. GRANGER, *Metall. Trans. A* **21A** (1990) 205.
33. H. JONES, *Phil. Mag. B* **61** (1990) 487.
34. M. C. FLEMINGS, in "Solidification Processing" edited by M. C. Flemings (McGraw-Hill, New York, 1974).

Received 28 July
and accepted 26 August 1998